X-ray reprocessing in accreting pulsar GX 301-2 observed with *Insight*-HXMT

L. Ji [●],[1]★ V. Doroshenko [●],[1,2] V. Suleimanov,[1,3,2] A. Santangelo,[1,4] M. Orlandini [●],[5] J. Liu,[6] L. Ducci,[1,7]
S. N. Zhang,[4,8] A. Nabizadeh [●],[9] D. Gavran,[1] S. Zhang,[4] M. Y. Ge,[4] X. B. Li,[4] L. Tao,[4] Q. C. Bu,[4,1]
J. L. Qu,[4] F. J. Lu,[4] L. Chen,[10] L. M. Song,[4,8] T. P. Li,[4,8,11] Y. P. Xu,[4,8] X. L. Cao,[4] Y. Chen,[4] C. Z. Liu,[4]
C. Cai,[4,8] Z. Chang,[4] T. X. Chen,[4] Y. P. Chen,[4] W. W. Cui,[4] Y. Y. Du,[4] G. H. Gao,[4,8] H. Gao,[4,8] Y. D. Gu,[4]
J. Guan,[4] C. C. Guo,[4,8] D. W. Han,[4] Y. Huang,[4,8] J. Huo,[4] S. M. Jia,[4] W. C. Jiang,[4] J. Jin,[4] L. D. Kong,[4,8]
B. Li,[4] C. K. Li,[4] G. Li,[4] W. Li,[4] X. Li,[4] X. F. Li,[4] Z. W. Li,[4] X. H. Liang,[4] J. Y. Liao,[4] B. S. Liu,[4]
H. X. Liu,[4,8] H. W. Liu,[4] X. J. Liu,[4] X. F. Lu,[4] Q. Luo,[4,8] T. Luo,[4] R. C. Ma,[4,8] X. Ma,[4] B. Meng,[4]
Y. Nang,[4,8] J. Y. Nie,[4] G. Ou,[4] X. Q. Ren,[4,8] N. Sai,[4,8] X. Y. Song,[4] L. Sun,[4] Y. Tan,[4] Y. L. Tuo,[4,8]
C. Wang,[4,8] L. J. Wang,[4] P. J. Wang,[4,8] W. S. Wang,[4] Y. S. Wang,[4] X. Y. Wen,[4] B. Y. Wu,[4,8] B. B. Wu,[4]
M. Wu,[4] G. C. Xiao,[4,8] S. Xiao,[4,8] S. L. Xiong,[4] R. J. Yang,[12] S. Yang,[4] Yan-Ji Yang,[4] Yi-Jung Yang,[4]
Q. B. Yi,[4,13] Q. Q. Yin,[4,8] Y. You,[4,8] F. Zhang,[4] H. M. Zhang,[4] J. Zhang,[4] P. Zhang,[4] W. Zhang,[4,8]
W. C. Zhang,[4] Yi Zhang,[4] Y. F. Zhang,[4] Y. H. Zhang,[4,8] H. S. Zhao,[4] X. F. Zhao,[4,8] S. J. Zheng,[4]
Y. G. Zheng[4,12] and D. K. Zhou[4,8]

[1] *Institut für Astronomie und Astrophysik, Kepler Center for Astro and Particle Physics, Eberhard Karls Universität, Sand 1, D-72076 Tübingen, Germany*
[2] *Space Research Institute of the Russian Academy of Sciences, Profsoyuznaya Str 84/32, Moscow 117997, Russia*
[3] *Astronomy Department, Kazan (Volga region) Federal University, Kremlevskaya str 18, 42008 Kazan, Russia*
[4] *Key Laboratory for Particle Astrophysics, Institute of High Energy Physics, Beijing 100049, China*
[5] *INAF – Osservatorio di Astrofisica e Scienza dello Spazio di Bologna, Via Piero Gobetti 101, I-40129 Bologna, Italy*
[6] *Beijing Planetarium, 138 Xizhimenwai Road, Beijing 100044, China*
[7] *ISDC Data Center for Astrophysics, Université de Genève, 16 chemin d'Écogia, CH-1290 Versoix, Switzerland*
[8] *Chinese Academy of Sciences, University of Chinese Academy of Sciences, Beijing 100049, China*
[9] *Department of Physics and Astronomy, University of Turku, FI-20014 Turku, Finland*
[10] *Department of Astronomy, Beijing Normal University, Beijing 100088, China*
[11] *Department of Astronomy, Tsinghua University, Beijing 100084, China*
[12] *College of Physics Sciences & Technology, Hebei University, No. 180 Wusi Dong Road, Lian Chi District, Baoding City, Hebei Province 071002 China*
[13] *School of Physics and Optoelectronics, Xiangtan University, Yuhu District, Xiangtan, Hunan 411105, China*

ABSTRACT
We investigate the absorption and emission features in observations of GX 301-2 detected with *Insight*-HXMT/LE in 2017–2019. At different orbital phases, we found prominent Fe Kα, Kβ, and Ni Kα lines, as well as Compton shoulders and Fe K-shell absorption edges. These features are due to the X-ray reprocessing caused by the interaction between the radiation from the source and surrounding accretion material. According to the ratio of iron lines (Kα and Kβ), we infer the accretion material is in a low ionization state. We find an orbital-dependent local absorption column density, which has a large value and strong variability around the periastron. We explain its variability as a result of inhomogeneities of the accretion environment and/or instabilities of accretion processes. In addition, the variable local column density is correlated with the equivalent width of the iron Kα lines throughout the orbit, which suggests that the accretion material near the neutron star is spherically distributed.

Key words: stars: neutron – X-rays: binaries – X-rays: individual: GX 301-2 .

1 INTRODUCTION

In high-mass X-ray binaries (HMXBs), the main component of the mass outflow emitted by the donor star and responsible for the X-ray

emission in the vicinity of the accreting compact object can be a spherically symmetric wind, a circumstellar disc, or a gas stream. The radiation, as seen from Earth, is absorbed both in the interstellar medium (ISM) and within the binary system. The latter is attributed to the accretion material that surrounds the compact star that is often inhomogeneous and highly clumpy as reflected by highly variable absorption. Absorption and re-emission of X-rays are affected by the

★ E-mail: ji.long@astro.uni-tuebingen.de

distribution of material and one of the key diagnostic tools to probe the environment in binary systems (e.g. Aftab, Paul & Kretschmar 2019). Fluorescence lines, especially of iron atoms, are prominent features of the X-ray reprocessing in HMXBs (see e.g. Torrejón et al. 2010; Tzanavaris & Yaqoob 2018). They are produced by the absorption of high-energy photons that remove K-shell electrons and lead to electronic transitions (L→K: Fe Kα and M→K: Fe Kβ; Kallman et al. 2004). In addition, when the compact star is embedded in a dense wind, the Compton scattering is non-negligible, which scatters a fraction of emissions out of the line of sight (LOS) and reduces the observed flux. On the other hand, the down-scattering of fluorescence lines may lead to the appearance of a 'Compton shoulder' (CS) due to electron recoils (Matt 2002; Watanabe et al. 2003).

GX 301-2 is an HMXB consisting of a highly magnetized ($B \sim 4 \times 10^{12}$ G, or even larger Doroshenko et al. 2010) pulsar and a B-type hyper-giant star Wray 977 (Vidal 1973; Kaper et al. 1995; Staubert et al. 2019). According to modelling of high-resolution optical spectra, Wray 977 has a mass of 43 ± 10 M$_{\odot}$, a radius of 62 R$_{\odot}$, and looses mass through powerful stellar winds at a rate of $\sim 10^{-5}$ M$_{\odot}$ yr^{-1} with terminal velocity of 300 km s^{-1} (Kaper, van der Meer & Najarro 2006). The system is highly eccentric ($e \sim 0.46$), with an orbital period of ~ 41.5 d, and exhibits strong variation of the X-ray flux with orbital phase (Koh et al. 1997; Doroshenko et al. 2010). In particular, periodic outbursts at the orbital phase ~ 1.4 d before the periastron passage (Sato et al. 1986), and a fainter one near the apastron passage are observed (Pravdo et al. 1995). The broad-band X-ray spectrum is orbital phase-dependent and can be approximately described as a power law with a high-energy cutoff and a cyclotron resonant scattering feature around 40 keV (Kreykenbohm et al. 2004; Mukherjee & Paul 2004; La Barbera et al. 2005; Doroshenko et al. 2010; Suchy et al. 2012; Islam & Paul 2014; Fürst et al. 2018; Nabizadeh et al. 2019). During the periastron flares, the source exhibits strong variability with an amplitude of up to a factor of 25, reaching a few hundreds mCrab in the energy band of 2–10 keV (e.g. Rothschild & Soong 1987; Pravdo et al. 1995). The flares are accompanied by the variability of the equivalent hydrogen column density ($N_{\rm H}$) and of the fluorescent iron lines, which is believed to be associated with clumpiness of the stellar wind, launched from the donor star (Mukherjee & Paul 2004). We note the *clumpiness* in this paper refers to any inhomogeneities in the stellar wind/stream, which are higher density regions, regardless of its specific formation mechanisms. On the other hand, Fürst et al. (2011) reported a long *XMM–Newton* observation in GX 301-2 around its periastron, which also exhibits systematic variations of the flux and $N_{\rm H}$ at a time-scale of a few kiloseconds. Several wind accretion models, consisting of stellar winds and a gas stream, were proposed to explain the observed flares (e.g. Haberl 1991; Leahy 1991; Leahy & Kostka 2008; Mönkkönen et al. 2020).

As already mentioned, reprocessing of X-ray emission can be used to probe the environment surrounding the neutron star. We note that, however, a comprehensive and detailed study of the X-ray reprocessing over the entire orbit is still missing. Thanks to the high cadence observations of *Insight-Hard X-ray Modulation Telescope* (*HXMT*; Zhang et al. 2020) in 2017–2019, we are able to study the X-ray reprocessing at different orbital phases, and compare it with the result of the flaring episode. This work aims at improving our understanding on the accretion environment of GX 301-2 by studying X-ray processing. This paper is organized as follows: In Section 2, we describe observations and procedures adopted for data reduction; the spectral analysis and results are represented in Section 3; we summarize our conclusions in Sections 4 and 5.

2 DATA REDUCTION

Insight-HXMT is the first Chinese X-ray satellite, which consists of three telescopes, i.e. the low-, medium-, and high-energy telescopes (Zhang et al. 2014, 2020). In this work, we only used the low-energy telescope (LE), which is made up of swept charge devices and cover the energy range of 1–10 keV. The broad-band spectral analysis will be published elsewhere, and here, we only focus on the narrow emission and absorption features (i.e. iron line complex) observed in the soft X-ray band, and associated them with reprocessing of X-ray emission by winds. LE has an energy resolution of 140 eV at 5.9 keV, and an effective area of 384 cm^2 (Chen et al. 2020). Thanks to its fast-readout, LE does not suffer from photon saturation and pile-up effects, and is therefore capable of observing strong sources, like the flaring state of GX 301-2. *Insight*-HXMT performed 67 pointing observations between 2017 and 2019, with an averaged exposure of $\sim$2000 s. However, in some cases, the observations were dominated by the background, especially when the source was faint, which precludes detailed spectral analysis. In particular, we only select the observations in which the source contributes to more than 25 per cent of the count rate between 1 and 10 keV, and the exposure is larger than 1000 s for the analysis. Here, the background was estimated by using LEBKGMAP, a PYTHON code that has been included in HXMTDAS-2.02.1. As a result, 23 observations have been selected in our sample, and their summary is shown in Table 1. We performed the data reduction of *Insight*-HXMT, following the official user guide[1]: the criteria for data screening is that the elevation angle > 10 degree; the geomagnetic cutoff rigidity > 8 GeV; the pointing offset angle < 0.1 degree; at least 300 s away from the South Atlantic Anomaly. During the spectral analysis, we used XSPEC V12.10, an X-ray spectral fitting package in HEASOFT V6.26 (Arnaud 1996). We assumed solar abundances (Wilms, Allen & McCray 2000), as suggested by previous observations (Torrejón et al. 2010). In this paper, we identified the existence of a component only if its detection is at a confidence level of > 3σ. The significance was estimated by Monte Carlo simulations performed by using SIMFTEST, a built-in script in XSPEC. A systematic error of the LE calibration (CALDB 2.02.01), regarding the energy-to-channel (E–C) relation, has been found recently,[2] which will lead to an overestimation of the line energy by a few tens of eV. Such a deviation is expected to be a constant observations. Therefore an offset of the E–C relation has been taken into account in our analysis (see below). All uncertainties in this paper correspond to a 68 per cent confidence level.

3 RESULTS

We focused on the energy band of 5.5–8.5 keV, where the emission and absorption features are expected from past observations of the source with *Chandra*/HEG (Watanabe et al. 2003; Torrejón et al. 2010; Tzanavaris & Yaqoob 2018). In this narrow energy band, the continuum can be described with a power-law spectral model. The model (M) we used is

$$M = \text{abs1}\left(N_{\rm H}^{\rm gal}\right) \times \left\{ \text{abs2}\left(N_{\rm H}^{\rm loc}\right) \times \text{cabs}\left(N_{\rm H}^{\rm loc}\right) \right.$$

$$\left. \times \text{powerlaw} + \text{Gaussian lines} + \text{box} \right\} \qquad (1)$$

---

[1]See http://enghxmt.ihep.ac.cn/SoftDoc/169.jhtml.
[2]Private communication with Dr. Xiaobo Li.

Table 1. The columns denote observational IDs, the observation date, the exposure, the orbital phase assuming the ephemeris adopted from Koh et al. (1997), and best-fitting parameters of the continuum that is described as an absorbed power-law model.

ObsID	Time (MJD)	Exposure (s)	Phase$_{orb}$	Γ	N_H^{loc} (10^{22} atoms cm^{-2})	Unabsorbed flux$_{5.5-8.5\,keV}$ (10^{-9} erg cm^{-2} s^{-1})
P010130900101	57968.33	1886	0.87	$0.95^{+0.06}_{-0.05}$	$95.64^{+4.04}_{-4.84}$	$6.39^{+0.57}_{-0.62}$
P010130900102	57968.46	2027	0.87	$1.22^{+0.13}_{-0.09}$	$93.57^{+4.25}_{-7.61}$	$3.81^{+0.35}_{-0.55}$
P010130900103	57968.60	1792	0.87	$1.31^{+0.07}_{-0.06}$	$125.18^{+4.62}_{-5.83}$	$9.18^{+0.95}_{-1.05}$
P010130900104	57968.73	1506	0.88	$2.53^{+0.09}_{-0.12}$	$211.48^{+4.74}_{-6.05}$	$11.65^{+1.19}_{-1.69}$
P010130900107	57969.15	2538	0.89	$1.29^{+0.08}_{-0.08}$	$114.35^{+6.09}_{-5.28}$	$4.30^{+0.59}_{-0.45}$
P010130900401	57969.58	1827	0.90	$1.89^{+0.07}_{-0.10}$	$128.83^{+8.45}_{-5.87}$	$2.53^{+0.45}_{-0.31}$
P010130900402	57969.73	1264	0.90	$1.15^{+0.03}_{-0.06}$	$66.68^{+2.02}_{-3.66}$	$4.16^{+0.15}_{-0.34}$
P010130900502	58121.32	1088	0.55	$2.10^{+0.06}_{-0.04}$	$18.84^{+3.06}_{-1.99}$	$0.41^{+0.02}_{-0.01}$
P010130900701	58137.54	1036	0.94	$1.73^{+0.02}_{-0.03}$	$80.65^{+0.31}_{-1.27}$	$0.95^{+0.02}_{-0.02}$
P010130900808	58148.71	2513	0.21	$1.58^{+0.01}_{-0.01}$	$57.67^{+0.52}_{-0.39}$	$0.63^{+0.01}_{-0.01}$
P010130900901	58163.01	2914	0.56	$2.45^{+0.02}_{-0.03}$	$50.16^{+3.40}_{-3.82}$	$0.46^{+0.05}_{-0.04}$
P010130901501	58218.03	7713	0.88	$1.33^{+0.06}_{-0.07}$	$150.24^{+4.73}_{-6.46}$	$7.74^{+0.81}_{-0.96}$
P010130901601	58258.34	1645	0.86	$1.13^{+0.08}_{-0.06}$	$113.93^{+5.38}_{-6.07}$	$7.11^{+0.87}_{-0.87}$
P010130901602	58258.50	1188	0.86	$1.84^{+0.09}_{-0.14}$	$201.33^{+5.39}_{-5.54}$	$13.02^{+2.01}_{-1.67}$
P010130901701	58259.83	1012	0.89	$2.51^{+0.19}_{-0.14}$	$167.21^{+14.86}_{-16.04}$	$3.95^{+1.38}_{-1.04}$
P010130901702	58259.96	1182	0.89	$1.99^{+0.15}_{-0.17}$	$170.67^{+8.03}_{-11.10}$	$4.25^{+1.08}_{-1.10}$
P010130901802	58327.04	1206	0.51	$1.67^{+0.03}_{-0.03}$	$30.82^{+2.00}_{-2.32}$	$0.40^{+0.03}_{-0.03}$
P010130901901	58494.92	2685	0.56	$1.42^{+0.03}_{-0.02}$	$35.83^{+2.27}_{-1.49}$	$1.98^{+0.11}_{-0.07}$
P010130902001	58495.75	3432	0.58	$1.48^{+0.02}_{-0.01}$	$47.04^{+1.45}_{-0.42}$	$2.38^{+0.06}_{-0.05}$
P010130902101	58545.36	2092	0.77	$2.00^{+0.08}_{-0.10}$	$41.14^{+4.12}_{-3.71}$	$0.69^{+0.05}_{-0.06}$
P010130902102	58545.49	2214	0.78	$1.54^{+0.01}_{-0.01}$	$40.69^{+0.30}_{-0.50}$	$1.06^{+0.01}_{-0.01}$
P010130902103	58545.63	2495	0.78	$1.46^{+0.04}_{-0.03}$	$54.69^{+2.97}_{-2.74}$	$2.34^{+0.14}_{-0.14}$
P010130902104	58545.79	2894	0.78	$1.28^{+0.02}_{-0.03}$	$51.10^{+2.67}_{-4.07}$	$2.61^{+0.13}_{-0.21}$

where

$$box = \begin{cases} norm, & when\ 6.24\,keV < E < 6.40\,keV \\ 0, & otherwise \end{cases} \quad (2)$$

, and abs1(N_H^{gal}) and abs2(N_H^{loc}) represent photoelectric absorption caused by the Galactic and local ISM, respectively. In practice, we adopt the tbnew[3] model to describe them. The N_H^{gal} was fixed at 1.4×10^{22} atoms cm^{-2} (HI4PI Collaboration 2016). The cabs[4] model was used to account for the Compton scattering that decreases the flux along the LOS. We note that our data can also be well described without inclusion of the cabs component which is coupled with the normalization of the powerlaw component and does not affect any of our conclusions. We also included several Gaussian lines to model fluorescent lines, and the line widths were fixed at 1 eV,[5] as suggested by *Chandra*/HEG. Only most prominent fluorescent lines, i.e. Fe Kα, Fe Kβ, and Ni Kα, were considered because of statistics. In addition, we found that sometimes the Fe Kα line deviates from the symmetric Gaussian line profile (see residuals in Fig. 1), which is likely due to the presence of a CS. To account for this feature, we also included a box-shaped function covering the energy range 6.24–6.40 keV (for details, see Matt 2002). We considered the presence of CSs only if the box function could improve the goodness of fit at a significant level of $> 3\sigma$ estimated by SIMFTEST. The model in equation (1) can well
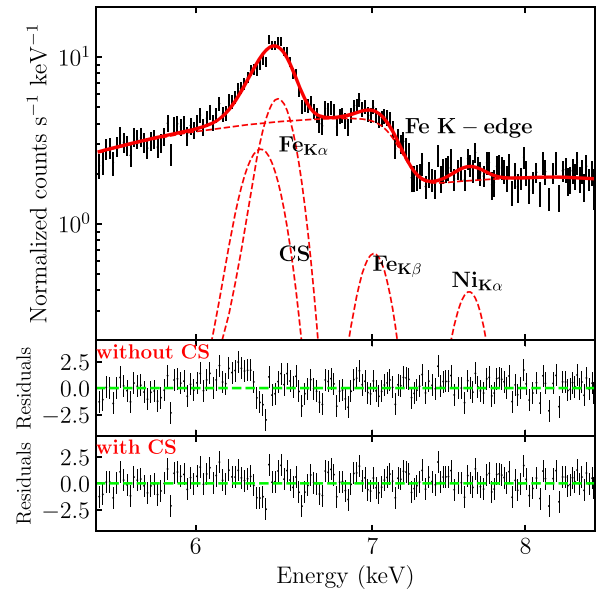

Figure 1. A representative spectrum of GX 301-2 in our sample (obsID:P010130901601; upper panel). The spectrum is fitted in the energy range of 5.5–8.5 keV with an absorbed (tbabs) powerlaw model including three emission lines, i.e. Fe Kα, Fe Kβ, and Ni Kα and an additional CS described as a box function. We show residuals with and without the CS component in the two bottom panels.

[3]https://pulsar.sternwarte.uni-erlangen.de/wilms/research/tbabs/
[4]https://heasarc.gsfc.nasa.gov/xanadu/xspec/manual/node234.html
[5]We confirmed that LE is not able to constrain the line widths and only upper limits can be obtained if setting up them free.

describe all spectra in our sample with an averaged reduced-χ^2 of 0.9 (269 dof), and we show a representative example in Fig. 1. As studied by Torrejón et al. (2010), recombination lines (Fe XXV and Fe XXVI) were also detected in some HMXBs. However, in our sample, we did not find signals of Fe XXV and Fe XXVI, which is consistent with the previous conclusion that recombination lines are not present in supergiant X-ray binaries (Giménez-García et al. 2015).

It has been known that the N_H^{loc} in GX 301-2 exhibits short-term and long-term variability (Mukherjee & Paul 2004; Fürst et al. 2011). The former is thought to be caused by the clumpiness of the accretion material, while the latter is attributed to the evolution of the accretion environment of stellar winds or the gas stream, as a function of the orbital phase. *Insight*-HXMT covered a substantial fraction of the orbit, which allows us to investigate the N_H^{loc} variability at different timescales. The results are presented in Fig. 2 and Table 2. As it is evident from the figure, N_H^{loc} is the largest and exhibits strongest variability around the orbital phase 0.9, when the flux is enhanced as well although it is important to emphasize that the local absorption column remains variable throughout the orbit. In addition, observational IDs having a same prefix (such as P0101309001∗) are parts of a long-pointed observation separated by short gaps, which allows us to study the N_H^{loc} variation at a short time-scale of a few kiloseconds. To conclude, the observed N_H^{loc} is significantly variable at this short time-scale, which indicates that the N_H^{loc} fluctuation in Fig. 2 is mainly caused by short-term effects. This result is well consistent with the long exposure *XMM*–Newton observation (Fürst et al. 2011).

The centroid energy of the Fe Kα line ($\sim$6.43 keV) appears to be consistent for all observations and corresponds to the ionization degree of more than Fe XVIII (Kallman et al. 2004). However, we note that the ionization state might be overestimated considering the optical depth of the absorber, and is inconsistent with previous reports (e.g. Watanabe et al. 2003; Fürst et al. 2011). On the other hand, if materials are ionized beyond Fe XVIII, the resulting photoionization threshold should be much higher (fig. 4(c) in Kallman et al. 2004), which is inconsistent with the fact that the data can be modelled with an absorption edge when assuming neutral ions (see below). We note that this discrepancy is likely caused by the systematic uncertainty of the E–C relation as mentioned above. Therefore, in practice, we fitted the spectrum of the first observation (ObsID:P010130900101), by freezing Fe Kα line at 6.4 keV and setting up the *gain offset*[6] free. The resulting offset was 35 eV, which, hereafter, was considered for other spectra.

The fitting results have been summarized and tabulated in Table 2. Similar to the N_H^{loc}, the Fe lines are also highly variable and related to the orbital phase (Fig. 2). Both the equivalent width (EW) and the flux of Fe Kα lines present large values and strong variability around the periastron. We show the linear relation between intensities of Fe Kβ and Kα lines in Fig. 3. A linear fitting leads to a linear coefficient of 0.12 ± 0.01. We note that, in theory, this coefficient is described as a function of the iron ionization state (see fig. 2 in Palmeri et al. 2003). Therefore, this result suggests a low ionization state (electron occupancy $\gtrsim$ 22) and is consistent with our assumption mentioned above. In Fig. 4, we represent the unabsorbed flux of the continuum in the energy range of 5.5–8.5 keV against the flux of Fe Kα/Kβ lines. Clearly, both of them are positively correlated, which is consistent with the relation among other sources (see fig. 6 in Giménez-García et al. 2015).
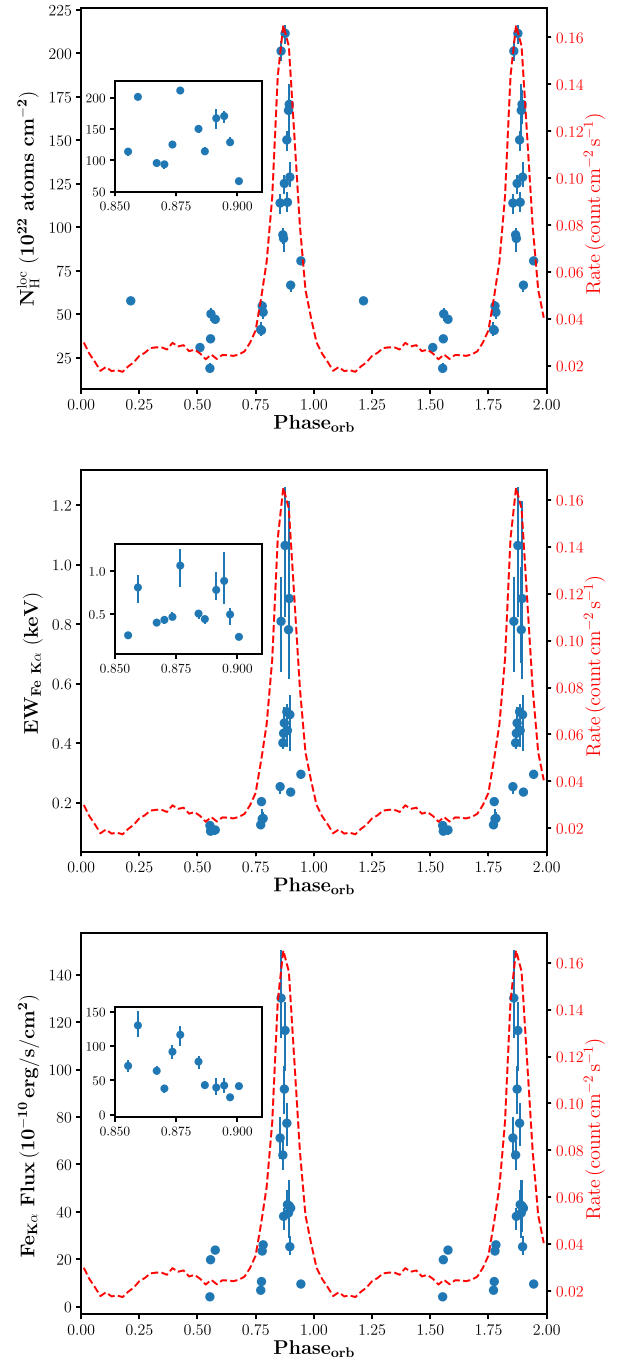
---

[6]For details, see https://heasarc.gsfc.nasa.gov/xanadu/xspec/manual/node99.html.

Figure 2. The equivalent local hydrogen column (N_H^{loc}) versus the orbital phase (upper panel). The inset is a zoom-in to show the significant N_H^{loc} variation around the orbital phase 0.9. The orbital modulation of the flux (red) is also superimposed, which is monitored by *Swift*/BAT in the energy range of 15–50 keV. Here, the binary ephemeris is adopted from Koh et al. (1997). We show orbital evolutions of EWs and intensities of Fe Kα lines in the middle and bottom panels.

Assuming that Fe Kα lines are emitted from a spherical shell of gas surrounding the source, the EW is expected to be related to the local hydrogen column density as $EW_{Fe\ K\alpha}(eV) \approx 3 \times 10^{-22} N_H^{loc}$, if considering a power-law continuum spectrum with a photon index (Γ) of 2 (Kallman et al. 2004; Inoue 1985). Therefore, we compared

Table 2. The parameters of emission and absorption features, i.e. the Fe Kα, Fe Kβ, Ni Kα, CS and the optical depth of the iron K-shell, where '–' represents features that can not be identified at 3σ confidence level.

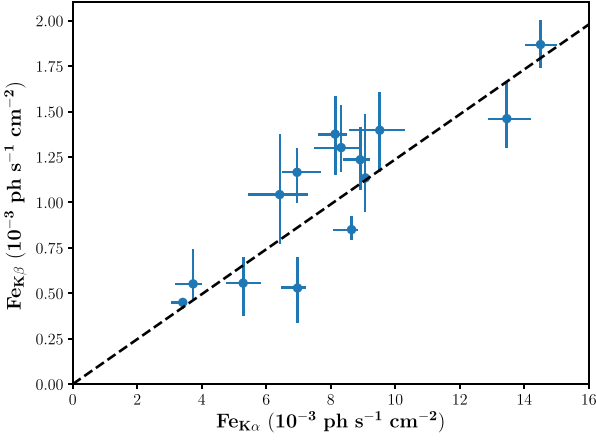| ObsID	τ_{Kedge} (MJD)	$E_{\mathrm{FeK\alpha}}$ (keV)	$EW_{\mathrm{FeK\alpha}}$ (eV)	$I_{\mathrm{FeK\alpha}}$ (10^{-3} photons cm^{-2} s^{-1})	$E_{\mathrm{FeK\beta}}$ (keV)	$EW_{\mathrm{FeK\beta}}$ (eV)	$I_{\mathrm{FeK\beta}}$ (10^{-3} photons cm^{-2} s^{-1})	$E_{\mathrm{NiK\alpha}}$ (keV)	$EW_{\mathrm{NiK\alpha}}$ (eV)	$I_{\mathrm{NiK\alpha}}$ (10^{-3} photons cm^{-2} s^{-1})	EW_{CS} (eV)
P010130900101	$0.89^{+0.03}_{-0.03}$	$6.406^{+0.002}_{-0.002}$	$400.86^{+23.18}_{-19.52}$	$14.51^{+0.50}_{-0.47}$	$7.05^{+0.02}_{-0.02}$	$64.64^{+4.74}_{-4.47}$	$1.87^{+0.14}_{-0.13}$	$7.48^{+0.02}_{-0.02}$	$42.13^{+15.68}_{-11.37}$	$0.82^{+0.30}_{-0.22}$	$58.91^{+8.94}_{-9.20}$
P010130900102	$0.87^{+0.05}_{-0.06}$	$6.398^{+0.001}_{-0.003}$	$433.10^{+25.67}_{-44.96}$	$8.92^{+0.30}_{-0.53}$	$6.99^{+0.02}_{-0.05}$	$66.68^{+10.98}_{-11.47}$	$1.24^{+0.18}_{-0.16}$	–	–	–	–
P010130900103	$1.18^{+0.04}_{-0.06}$	$6.404^{+0.003}_{-0.004}$	$467.61^{+50.95}_{-30.70}$	$13.46^{+0.73}_{-0.58}$	$7.00^{+0.03}_{-0.03}$	$58.84^{+8.63}_{-7.12}$	$1.46^{+0.21}_{-0.16}$	$7.50^{+0.03}_{-0.02}$	$55.73^{+19.02}_{-15.75}$	$0.76^{+0.26}_{-0.21}$	$40.08^{+10.53}_{-21.98}$
P010130900104	–	$6.396^{+0.006}_{-0.004}$	$1064.29^{+194.36}_{-240.46}$	$8.33^{+0.54}_{-0.85}$	$7.05^{+0.01}_{-0.01}$	$215.14^{+50.99}_{-26.55}$	$1.30^{+0.23}_{-0.13}$	–	–	–	$42.97^{+60.68}_{-28.41}$
P010130900107	$0.98^{+0.05}_{-0.05}$	$6.400^{+0.007}_{-0.003}$	$442.36^{+29.14}_{-53.19}$	$6.97^{+0.24}_{-0.51}$	$7.02^{+0.03}_{-0.04}$	$37.94^{+13.60}_{-14.54}$	$0.53^{+0.17}_{-0.19}$	$7.55^{+0.04}_{-0.04}$	$79.51^{+22.22}_{-22.52}$	$0.66^{+0.18}_{-0.20}$	–
P010130900401	–	$6.402^{+0.014}_{-0.007}$	$495.75^{+65.23}_{-120.75}$	$3.74^{+0.28}_{-0.56}$	$6.99^{+0.03}_{-0.04}$	$86.14^{+33.57}_{-16.97}$	$0.55^{+0.19}_{-0.10}$	–	–	–	–
P010130900402	$0.68^{+0.06}_{-0.06}$	$6.401^{+0.007}_{-0.008}$	$235.38^{+1.94}_{-1.73}$	$9.08^{+0.04}_{-0.04}$	$6.95^{+0.03}_{-0.02}$	$32.81^{+10.99}_{-5.45}$	$1.13^{+0.35}_{-0.19}$	–	–	–	–
P010130900502	–	$6.430^{+0.039}_{-0.035}$	$123.02^{+6.78}_{-4.63}$	$1.23^{+0.04}_{-0.04}$	–	–	–	–	–	–	–
P010130900701	$0.70^{+0.01}_{-0.01}$	$6.404^{+0.020}_{-0.022}$	$295.17^{+3.30}_{-13.56}$	$1.93^{+0.04}_{-0.02}$	–	–	–	–	–	–	–
P010130900808	$0.44^{+0.01}_{-0.01}$	–	–	–	–	–	–	–	–	–	–
P010130900901	–	–	–	–	–	–	–	–	–	–	–
P010130901501	$1.40^{+0.01}_{-0.01}$	$6.401^{+0.005}_{-0.002}$	$505.54^{+26.39}_{-57.16}$	$8.65^{+0.20}_{-0.56}$	$7.00^{+0.04}_{-0.02}$	$64.79^{+6.09}_{-4.79}$	$0.85^{+0.07}_{-0.06}$	–	–	–	$95.17^{+22.09}_{-17.78}$
P010130901601	$0.92^{+0.01}_{-0.01}$	$6.419^{+0.008}_{-0.004}$	$253.64^{+14.80}_{-24.17}$	$8.14^{+0.35}_{-0.53}$	$6.95^{+0.04}_{-0.03}$	$56.02^{+9.05}_{-9.78}$	$1.38^{+0.21}_{-0.22}$	$7.57^{+0.03}_{-0.03}$	$48.06^{+21.35}_{-18.41}$	$0.68^{+0.30}_{-0.25}$	$132.77^{+16.62}_{-14.12}$
P010130901602	–	$6.410^{+0.008}_{-0.004}$	$809.40^{+145.68}_{-170.49}$	$9.52^{+0.78}_{-0.95}$	$7.07^{+0.03}_{-0.03}$	$174.01^{+30.09}_{-28.41}$	$1.40^{+0.21}_{-0.23}$	–	–	–	$84.41^{+65.98}_{-36.60}$
P010130901701	–	$6.417^{+0.003}_{-0.005}$	$781.20^{+210.39}_{-111.72}$	$6.96^{+0.73}_{-0.47}$	$7.05^{+0.03}_{-0.03}$	$249.79^{+31.16}_{-30.64}$	$1.17^{+0.13}_{-0.16}$	–	–	–	$143.52^{+33.87}_{-46.35}$
P010130901702	–	$6.395^{+0.008}_{-0.008}$	$886.00^{+326.83}_{-270.04}$	$6.42^{+0.88}_{-0.97}$	$7.00^{+0.02}_{-0.01}$	$211.27^{+91.89}_{-67.37}$	$1.04^{+0.33}_{-0.27}$	–	–	–	$91.75^{+110.96}_{-68.99}$
P010130901802	–	–	–	–	–	–	–	–	–	–	–
P010130901901	$0.35^{+0.06}_{-0.04}$	$6.419^{+0.019}_{-0.003}$	$104.02^{+1.00}_{-1.08}$	$3.49^{+0.06}_{-0.03}$	–	–	–	–	–	–	–
P010130902001	$0.33^{+0.04}_{-0.06}$	$6.396^{+0.013}_{-0.015}$	$108.07^{+3.67}_{-14.49}$	$3.41^{+0.09}_{-0.37}$	$7.03^{+0.01}_{-0.01}$	$16.49^{+0.38}_{-1.29}$	$0.45^{+0.01}_{-0.03}$	–	–	–	–
P010130902101	–	$6.452^{+0.031}_{-0.029}$	$125.40^{+4.45}_{-4.31}$	$1.46^{+0.04}_{-0.05}$	–	–	–	–	–	–	–
P010130902102	$0.47^{+0.02}_{-0.01}$	$6.415^{+0.011}_{-0.009}$	$203.40^{+1.47}_{-1.20}$	$3.23^{+0.00}_{-0.00}$	–	–	–	–	–	–	–
P010130902103	$0.45^{+0.06}_{-0.05}$	$6.428^{+0.026}_{-0.020}$	$145.22^{+31.36}_{-34.21}$	$4.07^{+0.68}_{-0.80}$	–	–	–	–	–	–	–
P010130902104	$0.41^{+0.02}_{-0.02}$	$6.431^{+0.012}_{-0.013}$	$146.87^{+20.20}_{-17.03}$	$5.29^{+0.57}_{-0.52}$	$7.12^{+0.04}_{-0.04}$	$20.69^{+5.36}_{-6.30}$	$0.56^{+0.14}_{-0.18}$	–	–	–	$77.85^{+13.12}_{-16.62}$

Figure 3. Strengths of Fe Kα and Fe Kβ lines, and their linear relation (the black dashed line).
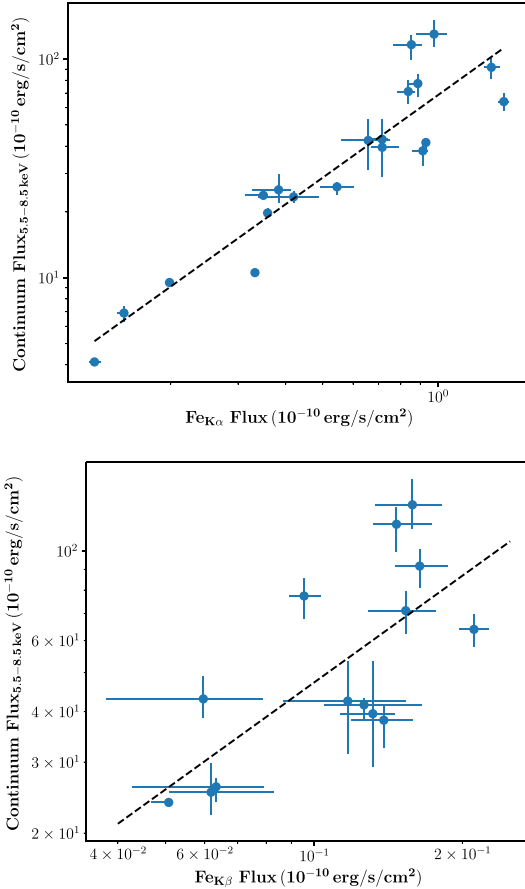

Figure 4. The upper (lower) panel shows the relation between the Fe Kα (Fe Kβ) flux and the unabsorbed flux of the continuum in the energy range of 5.5–8.5 keV. Dashed lines represent linear fits in the logarithmic space, which result in linear coefficients of 1.25 and 0.88 for Fe Kα and Fe Kβ lines, respectively.

our observations with the theoretical prediction shown in the upper panel of Fig. 5. Since the photon index does not strictly equalize to two in real observations, we included a correction factor $f(\Gamma)$, i.e. a normalization factor with respect to the case of $\Gamma=2$ (Endo et al.

Figure 5. The upper (bottom) panel shows EWs of Fe Kα lines (CSs) as a function of the local absorption column $N_{\mathrm{H}}^{\mathrm{loc}}$. The black dashed line represents the theoretical estimation [EW$_{\mathrm{Fe\ K}\alpha}$(eV) $\approx 3 \times 10^{-22} N_{\mathrm{H}}$] assuming a spherical shell of gas surrounding a point source of continuum radiation (Kallman et al. 2004).

2002), where

$$f(\Gamma) = \frac{\int_{E_{\mathrm{th}}}^{\infty} E^{-2} \sigma_{\mathrm{Fe}}(E) \mathrm{d}E}{\int_{E_{\mathrm{th}}}^{\infty} E^{-\Gamma} \sigma_{\mathrm{Fe}}(E) \mathrm{d}E} \qquad (3)$$

Here, E_{th} is the photoionization threshold energy, and σ_{Fe} is the K-shell photoionization cross-section. In spite of some scattering points, the EW significantly increases with the increasing of $N_{\mathrm{H}}^{\mathrm{loc}}$, which is generally in agreement with the theoretical estimation. The slight departure from the expected linear relationship, e.g. for the points with large $N_{\mathrm{H}}^{\mathrm{loc}}$ values, might be a hint of the aspherical accretion, such as the formation of the accretion disc suggested by Mönkkönen et al. (2020).

In nine out of 23 observations, the CS appears to be statistically significant. We show the relation between the EW of this component and the corresponding $N_{\mathrm{H}}^{\mathrm{loc}}$ in the bottom panel of Fig. 5. No apparent correlation can be identified due to the large scatter of individual data points. Considering the strong dependency between CSs and strong Fe Kα lines, we caution that such a scattering might be due to the imperfect description of observed features with simplified spectral models. Further observations with a better energy resolution are strongly encouraged in the future.
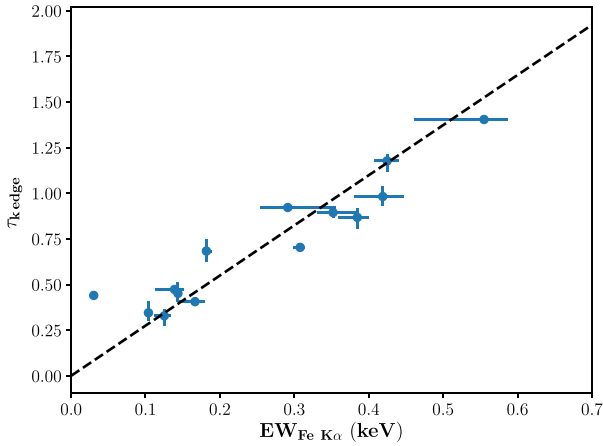
Figure 6. The relationship between the EW of the iron K_α line and the optical depth of the iron K-edge absorption, where the black line represents a linear fitting.

As shown in Fig. 1, a flux decrease is visible around 7 keV, which is attributed to the K-shell photoionization. It is useful to determine the relation between N_H^{loc} and the absorption optical depth. We performed an additional spectral analysis using the same model mentioned above but setting up the iron abundance of 'abs2' at 0. In addition, we included a phenomenological model, i.e. 'edge'[7] in XSPEC, to describe the absorption structure. There are two parameters in the 'edge' model, the threshold energy (E_c) and the absorption optical depth ($\tau_{K\,edge}$). To avoid the coupling with Fe $K\beta$ lines that are around 7 keV, we fixed E_c at 7.11 keV,[8] i.e. the predicted value for neutral irons. We show the relation and a linear fitting, i.e. $\tau_{K\,edge} = (2.5 \pm 0.4) \frac{EW_{Fe\,K\alpha}}{1\,keV}$, in Fig. 6. This relation suggests that the reprocessing material reaches an optical depth unit for EW $\sim$ 400 eV.

4 DISCUSSION

As illustrated in Fig. 2, a strong variability of the local absorption column at all orbital phases is revealed by *Insight*-HXMT observations. In general, the N_H^{loc} shows a considerable increase close to the periastron ($\phi = 0.9$) of the binary system, which is consistent with previous reports (e.g. Haberl 1991; Mukherjee & Paul 2004). Several models have been proposed to explain the observed dependence of both the absorbtion and flux on the orbital phase (Stevens 1988; Haberl 1991; Leahy 1991; Leahy & Kostka 2008; Mönkkönen et al. 2020). It is generally believed that the pulsar accretes matters both via a spherically symmetric wind (Castor, Abbott & Klein 1975) and focused accretion stream with a higher density. The latter is believed to be due to the enhanced mass loss on the surface of the supergiant star towards the neutron star, resulting in an Archimedes spiral-like structure because of the conservation of angular momentum (Leahy & Kostka 2008). We note that, although such a hybrid model can successfully reproduce the flux modulation of this source, the expected maximum of N_H^{loc} is at the orbital phase $\phi = 0.2$, which is inconsistent both with the *RXTE* results and our observations (fig. 6 in Leahy & Kostka 2008). On the other hand, the presence of the accretion stream itself with a shape similar to that deduced by Leahy

& Kostka (2008) has been directly confirmed through near-infrared interferometry (see i.e. fig. 13 in Waisberg et al. 2017), which might suggest that the observed absorption is not strongly affected by global distribution of matter within the binary system and is mostly local. This conclusion is also supported by the fact that the local absorption column observed by *Insight*-HXMT is strongly variable on short time-scales at all orbital phases, which is also consistent with reports from the literature (Mukherjee & Paul 2004; Fürst et al. 2011).

In general, two possible interpretations have been discussed in the literature to account for the observed variability of N_H^{loc} in HMXBs: wind clumps due to the line-deshadowing instability (e.g. MacGregor, Hartmann & Raymond 1979; Owocki & Rybicki 1984; Owocki, Castor & Rybicki 1988), and accretion instabilities in vicinity of a compact object. For instance, for GX 301–2, the former scenario was considered by Mukherjee & Paul (2004). On the other hand, recently El Mellah et al. (2020) suggested that the clumpiness of the stellar wind is likely not sufficient to explain such a large N_H^{loc} variation.

Alternatively, if the N_H^{loc} is mainly contributed by the material close to the neutron star (see below), the N_H^{loc} variability could originate from some instabilities in accretion processes appearing in hydrodynamic simulations (Blondin, Stevens & Kallman 1991; Manousakis, Walter & Blondin 2014; El Mellah et al. 2020). The dynamical time-scale of the accretion is $R_{acc}/v \sim 6$ ks, which is well consistent with the observed timescales of both the flux and N_H^{loc} variability (Fürst et al. 2011). $R_{acc} = \frac{2GM}{v^2} \sim 2.5 \times 10^9$ m is the accretion radius, i.e. the impact parameter of streamlines gravitationally beamed by the neutron star. Here, G is the gravitational constant, M is the mass of the neutron star, and v is the velocity of the flow before it is altered by the neutron star (Edgar 2004). The v is a function of the terminal velocity (v_∞) of the stellar wind and the velocity of the orbital movement. In GX 301-2, the v is $\sim$400 km s^{-1} around the periastron (Doroshenko et al. 2010).

We note that the absorbing material is also expected to be responsible for reprocessing of X-ray emission, and in particular contribute to the formation of fluorescent iron lines. Thanks to the good energy resolution of *Insight*-HXMT/LE and its high-cadence observational strategy, we are able to study the correlation of the N_H^{loc} with and the EW of iron $k\alpha$ lines (EW$_{Fe\,\alpha}$), at different orbital phases. We find that their correlation is well consistent with the theoretical prediction, if assuming that the iron line originates from X-ray reprocessing of hard X-rays with the accretion material surrounding the neutron star in approximately spherically symmetric geometry. This strongly suggests that same material is responsible both for absorption and X-ray reprocessing, which is consistent with results in supergiant X-ray binaries as reported by Giménez-García et al. (2015). The origin of the iron line (i.e. whether it forms close to the neutron star or on larger scales), however, is also still uncertain, and we discuss two possibilities here.

Based on the observed line width, Endo et al. (2002) proposed that it might be close to the Alfvén radius of the neutron star ($\sim 10^8$ m). In this case, the approximate spherical configuration (resembling an 'atmosphere') of accretion matter is expected (Davies, Fabian & Pringle 1979; Davies & Pringle 1981), which is consistent with the observed EW$_{Fe\,\alpha}$–N_H^{loc} relation revealed by our observations as described above. On the other hand, Zheng, Liu & Gou (2020) deduced somewhat longer distance ($1.2 \pm 0.6 \times 10^{10}$ m) to the iron line emitting region, based on the cross-correlation between light curves of the iron line and the continuum. If true, the N_H variability might be caused by the large structure of the accretion stream. However, there might be a problem that how to keep a spherical symmetry of matter at such a large scale.

We note that, in either case, according to the $\mathrm{EW}_{\mathrm{Fe}\alpha}-N_{\mathrm{H}}^{\mathrm{loc}}$ relation, the variability of the $N_{\mathrm{H}}^{\mathrm{loc}}$ cannot be caused by a dense clump moving through the LOS far away from the neutron star. We note also that observed variations of the local absorption column are largely driven by short-term variations, and correlation of the iron line EW and local absorption column also holds in this case as revealed both by *Insight*-HXMT and *XMM–Newton* observations during a flaring episode (fig. 12 in Fürst et al. 2011). This indicates that both the absorbing and re-processing material are located close to the neutron star and global spatial distribution of the accreting material does not play an important role in iron line and local absorption column properties, regardless on whether accretion proceeds from wind or accretion stream (e.g. Leahy & Kostka 2008; Mönkkönen et al. 2020). Enhancement of the local absorption column close to the periastron passage coincident with the increase of X-ray flux could in this case be explained by increased local wind density around the neutron star.

It is interesting to note also that for spherically symmetric distribution of reprocessing material, a significantly reduced pulse fraction is predicted in the energy range around the Fe Kα line complex. Indeed, in this case, the X-ray reprocessing only produces non-pulsed radiation, thereby reducing the total pulsed fraction. This inference is generally consistent with observations (e.g. fig. 5 in Nabizadeh et al. 2019). We note that a large size ($\gg$700 ls) of the line-forming region suggested by Suchy et al. (2012) is therefore not required. On the other hand, Liu et al. (2018) reported pulsed iron line in a time interval of 7 ks near the periastron, which disappeared afterwards. They explained that the intermittent pulsed iron line is associated with the anisotropic accretion, e.g. when going into or leaving the accretion stream. We note, however, that also in this case the asymmetry of reprocessing material may be local to the neutron star, i.e. be associated with an accretion wake or other features associated with interaction of the pulsar and the wind.

5 SUMMARY

We studied the emission and absorption features of accreting X-ray pulsar GX 301-2 observed with *Insight*-HXMT in 2017–2019. We found prominent fluorescent lines of Fe Kα, Fe Kβ and Ni Kα, and the K-shell absorption of irons, in observations at its different orbital phases. Our results show the capacity of *Insight*-HXMT in the context of iron complex studies on several timescales associated with good energy resolution and the fast read-out that prevents pile-up effects. We find that the Fe lines are orbital-dependent and their fluxes are correlated with those of the continuum. We report on the first extensive study of the intensity ratio between Fe Kα and Kβ lines in GX 301-2. In particular, we find a linear coefficient is 0.12 ± 0.01 between them, which is in a good agreement with the theoretical prediction of irons with a low ionization state (Palmeri et al. 2003).

We find that in GX 301-2, the optical depth of the K-shell absorption of irons is correlated to $\mathrm{EW}_{\mathrm{Fe}\alpha}$ with a linear coefficient of 2.5 ± 0.4. This coefficient is smaller than the result of *Chandra*, which is ~ 0.5 (Torrejón et al. 2010). We note that the discrepancy might be caused by the influence of Fe Kβ lines that cannot be resolved by *Insight*-HXMT.

CS previously reported based on the *Chandra* data (Watanabe et al. 2003; Torrejón et al. 2010; Tzanavaris & Yaqoob 2018) is significantly detected in several observations but find no clear relation with $N_{\mathrm{H}}^{\mathrm{loc}}$. We caution that, however, the energy resolution of *Insight*-HXMT/LE is not sufficient to fully resolve shape of the iron line complex and observations with grating or micro-calorimeter instruments are required to verify our conclusion.

We find also strong variations of the observed absorption column $N_{\mathrm{H}}^{\mathrm{loc}}$ both on short and long timescales. In particular, the absorption is significantly enhanced around the periastron passage which is consistent with earlier studies (e.g. Mukherjee & Paul 2004; La Barbera et al. 2005; Islam & Paul 2014). For the first time, we studied also the relation between $N_{\mathrm{H}}^{\mathrm{loc}}$ and $\mathrm{EW}_{\mathrm{Fe}\alpha}$ measured at different orbital phases in GX 301-2. We find that it is in line with a theoretical estimation assuming that the accretion material is distributed spherically, regardless of specific accretion types, i.e. via stellar winds or a gas stream (Leahy & Kostka 2008; Mönkkönen et al. 2020). We argue that together with rapid variations of both the $N_{\mathrm{H}}^{\mathrm{loc}}$ and iron line amplitude, this suggests that same material located close to the neutron star is likely responsible for both the absorption and X-ray reprocessing. We suggest, therefore, that rapid variability of the observed $N_{\mathrm{H}}^{\mathrm{loc}}$ is likely associated with inhomogenities and/or instabilities of the accretion flow around the neutron star. This conclusion is important in context of modelling of the observed orbital variation of X-ray flux and absorption column which shall thus be mostly considered as a tracer of local density around the pulsar rather than integral density of material along the LOS.

DATA AVAILABILITY

The data that support the findings of this study are available from *Insight*-HMXT's data archive[9] and the *Swift*/BAT transient monitor.[10]

REFERENCES

Aftab N., Paul B., Kretschmar P., 2019, ApJS, 243, 29
Arnaud K. A., 1996, in Jacoby G. H., Barnes J., eds, Astronomical Data Analysis Software and Systems V, ASP Conf. Ser. Vol.101, San Francisco, p. 17
Blondin J. M., Stevens I. R., Kallman T. R., 1991, ApJ, 371, 684

[9] http://enghxmt.ihep.ac.cn/
[10] https://swift.gsfc.nasa.gov/results/transients/

Castor J. I., Abbott D. C., Klein R. I., 1975, ApJ, 195, 157
Chen Y. et al., 2020, SCPMA, 63, 249505
Davies R. E., Pringle J. E., 1981, MNRAS, 196, 209
Davies R. E., Fabian A. C., Pringle J. E., 1979, MNRAS, 186, 779
Doroshenko V., Santangelo A., Suleimanov V., Kreykenbohm I., Staubert R., Ferrigno C., Klochkov D., 2010, A&A, 515, A10
Edgar R., 2004, New Astron. Rev., 48, 843
El Mellah I., Grinberg V., Sundqvist J. O., Driessen F. A., Leutenegger M. A., 2020, A&A, 643, 9
Endo T., Ishida M., Masai K., Kunieda H., Inoue H., Nagase F., 2002, ApJ, 574, 879
Fürst F. et al., 2011, A&A, 535, A9
Fürst F. et al., 2018, A&A, 620, A153
Giménez-García A., Torrejón J. M., Eikmann W., Martínez-Núñez S., Oskinova L. M., Rodes-Roca J. J., Bernabéu G., 2015, A&A, 576, A108
Haberl F., 1991, ApJ, 376, 245
HI4PI Collaboration, 2016, A&A, 594, A116
Inoue H., 1985, Space Sci. Rev., 40, 317
Islam N., Paul B., 2014, MNRAS, 441, 2539
Kallman T. R., Palmeri P., Bautista M. A., Mendoza C., Krolik J. H., 2004, ApJS, 155, 675
Kaper L., Lamers H. J. G. L. M., Ruymaekers E., van den Heuvel E. P. J., Zuiderwijk E. J., 1995, A&A, 300, 446
Kaper L., van der Meer A., Najarro F., 2006, A&A, 457, 595
Koh D. T. et al., 1997, ApJ, 479, 933
Kreykenbohm I., Wilms J., Coburn W., Kuster M., Rothschild R. E., Heindl W. A., Kretschmar P., Staubert R., 2004, A&A, 427, 975
La Barbera A., Segreto A., Santangelo A., Kreykenbohm I., Orlandini M., 2005, A&A, 438, 617
Leahy D. A., 1991, MNRAS, 250, 310
Leahy D. A., Kostka M., 2008, MNRAS, 384, 747
Liu J., Soria R., Qiao E., Liu J., 2018, MNRAS, 480, 4746
MacGregor K. B., Hartmann L., Raymond J. C., 1979, ApJ, 231, 514
Manousakis A., Walter R., Blondin J., 2014, in EPJ Web Conf. vol. 64, p. 02006(arXiv:1310.8205)

Matt G., 2002, MNRAS, 337, 147
Mönkkönen J., Doroshenko V., Tsygankov S. S., Nabizadeh A., Abolmasov P., Poutanen J., 2020, MNRAS, 494, 2178
Mukherjee U., Paul B., 2004, A&A, 427, 567
Nabizadeh A., Mönkkönen J., Tsygankov S. S., Doroshenko V., Molkov S. V., Poutanen J., 2019, A&A, 629, A101
Owocki S. P., Rybicki G. B., 1984, ApJ, 284, 337
Owocki S. P., Castor J. I., Rybicki G. B., 1988, ApJ, 335, 914
Palmeri P., Mendoza C., Kallman T. R., Bautista M. A., Meléndez M., 2003, A&A, 410, 359
Pravdo S. H., Day C. S. R., Angelini L., Harmon B. A., Yoshida A., Saraswat P., 1995, ApJ, 454, 872
Rothschild R. E., Soong Y., 1987, ApJ, 315, 154
Sato N., Nagase F., Kawai N., Kelley R. L., Rappaport S., White N. E., 1986, ApJ, 304, 241
Staubert R. et al., 2019, A&A, 622, A61
Stevens I. R., 1988, MNRAS, 235, 523
Suchy S., Fürst F., Pottschmidt K., Caballero I., Kreykenbohm I., Wilms J., Markowitz A., Rothschild R. E., 2012, ApJ, 745, 124
Torrejón J. M., Schulz N. S., Nowak M. A., Kallman T. R., 2010, ApJ, 715, 947
Tzanavaris P., Yaqoob T., 2018, ApJ, 855, 25
Vidal N. V., 1973, ApJ, 186, L81
Waisberg I. et al., 2017, ApJ, 844, 72
Watanabe S. et al., 2003, ApJ, 597, L37
Wilms J., Allen A., McCray R., 2000, ApJ, 542, 914
Zhang S. et al., 2014, Proc. Soc. Photo-Opt. Instrum. Eng., 9144, 914455
Zhang S. et al., 2020, SCPMA, 63, 249502
Zheng X., Liu J., Gou L., 2020, MNRAS, 491, 4802

This paper has been typeset from a TEX/LATEX file prepared by the author.